



Thickness-ultrathin and bismuth-rich strategies for BiOBr to enhance photoreduction of CO₂ into solar fuels



Liqun Ye^{a,b,d,*}, Xiaoli Jin^a, Chuan Liu^c, Chenghua Ding^a, Haiquan Xie^{a,**}, Ka Him Chu^b, Po Keung Wong^{b,**}

^a College of Chemistry and Pharmaceutical Engineering, Nanyang Normal University, Nanyang 473061, China

^b School of Life Sciences, The Chinese University of Hong Kong, Shatin, NT, Hong Kong SAR, China

^c College of Chemistry and Materials Engineering, Anhui Science and Technology University, Fengyang, 233100 Anhui Province, China

^d College of Petroleum and Natural Gas Engineering, Southwest Petroleum University, Chengdu 610500, China

ARTICLE INFO

Article history:

Received 16 November 2015

Received in revised form 14 January 2016

Accepted 18 January 2016

Available online 21 January 2016

Keywords:

Bi₄O₅Br₂

Ultrathin

Bismuth-rich

CO₂ conversion

Solar fuels

ABSTRACT

Two dimension layered BiOX (X = Cl, Br, I) semiconductor nanomaterials are very important photocatalysts. Our previous work showed that thickness-ultrathin and bismuth-rich strategies are excellent methods to improve the visible-light-driven (VLD) photocatalytic reduction activity of BiOX. In this study, thickness-ultrathin and bismuth-rich strategies were ingeniously combined to enhance the photocatalytic performance of the photocatalyst, via a glycerol precursor route, Bi₄O₅Br₂ microspheres assembled by ultrathin nanosheets was synthesized and characterized by X-ray diffraction (XRD) patterns, X-ray photoelectron spectroscopy (XPS), scanning electron microscope (SEM), energy dispersive spectrometer (EDS), high-resolution transmission electron microscopy (HRTEM), time-resolved PL spectra and UV–vis diffuse reflectance spectra (DRS). The thickness of Bi₄O₅Br₂ ultrathin nanosheets was about 3.7 nm, which was much thinner than the common BiOBr nanosheets (65 nm). Due to the thickness-ultrathin and bismuth-rich strategies, the synthesized Bi₄O₅Br₂ sample displayed a higher photocatalytic reduction activity of CO₂ conversion than BiOBr and ultrathin BiOBr under visible-light irradiation. More importantly, we found that thickness-ultrathin and bismuth-rich strategies played different roles. Thickness-ultrathin strategy only can increase the CO generation while bismuth-rich strategy only can increase the CH₄ generation for photoreduction of CO₂.

© 2016 Elsevier B.V. All rights reserved.

1. Introduction

The escalating environment and energy crises, which is partially due to the increasing atmospheric CO₂ concentration caused by the consumption of fossil fuels [1,2], is threatening human existence and development. Semiconductor photocatalytic technology has been suggested as an environmental friendly method to convert CO₂ into fuels and to remediate global warming [3–5]. Therefore, the development of semiconductor photocatalysis is influential to the progress of human development. Being the most important part of photocatalysis, photocatalytic materials decide the photocatalytic activity [6,7]. At present, the traditional photocatalysts such

as TiO₂ and ZnO showed very low photocatalytic activity under visible-light irradiation due to their wide band gaps [8,9]. In order to enhance the utilization of sunlight, many new visible-light-driven (VLD) photocatalysts were developed [10,11].

As an alternative photocatalysts to TiO₂ and ZnO, BiOX (X = Cl, Br, I) displays high photocatalytic activity due to their layered structure [12]. In previous studies, Zhang, Huang and Zan et al. have reported many exciting achievements in three following aspects [13–15]. Firstly, they developed a series of synthesis methods to prepare two-dimensional (2D) BiOX nanosheets and three-dimensional (3D) BiOX structure assembled with 2D nanoplates [16,17]. Secondly, they found that the facet effect for photocatalytic degradation of anoxic pollutant [18–20]. Thirdly, they modified BiOX to improve their photocatalytic activity through different ways such as surface plasmon resonance effect [21], sensitization [22], defect effect [23], doping [24] and coupling [25]. Their studies implied that the thickness of 2D BiOX nanosheets along [001] direction controlled the internal electric fields intensity and defect concentration. For example, ultrathin BiOCl nanosheets (ca. 3 nm)

* Corresponding author at: College of Chemistry and Pharmaceutical Engineering, Nanyang Normal University, Nanyang 473061, China.

** Corresponding authors.

E-mail addresses: yeliqun@163.com (L. Ye), xie-hq@163.com (H. Xie), pkwong@cuhk.edu.hk (P.K. Wong).

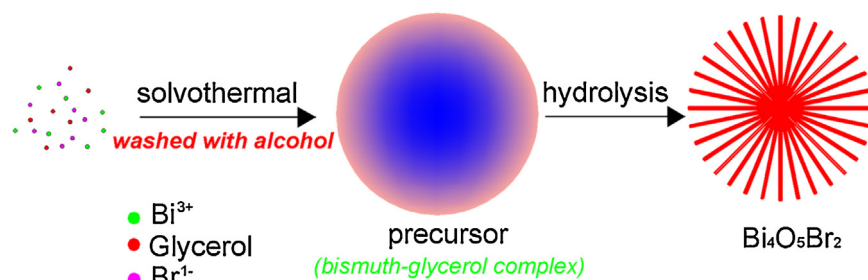


Fig. 1. Synthesis process of $\text{Bi}_4\text{O}_5\text{Br}_2$ glycerol precursor route.

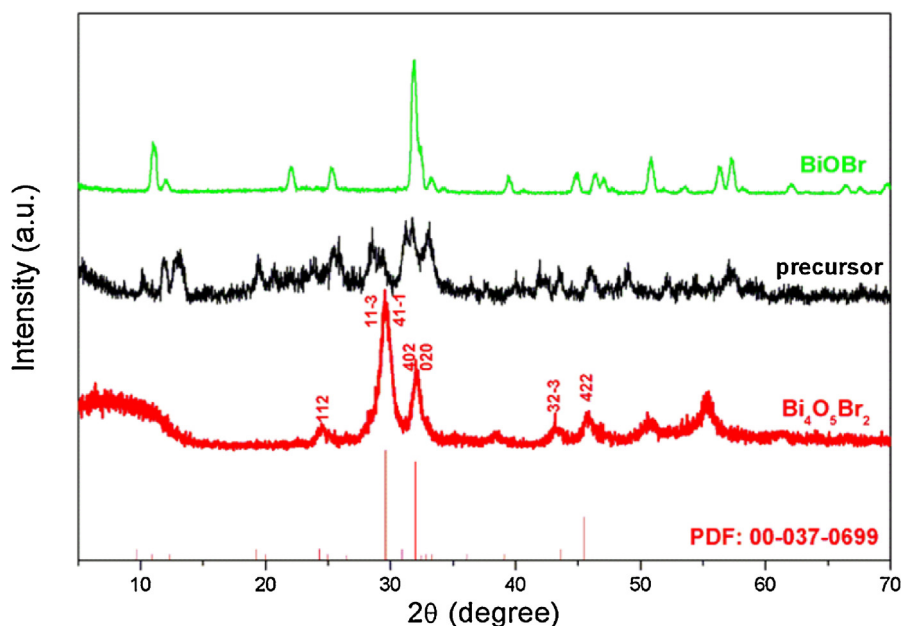


Fig. 2. XRD patterns of complex precursor, $\text{Bi}_4\text{O}_5\text{Br}_2$ and BiOBr .

had a large number of defects and showed high photocatalytic activity [26]. Therefore, the photocatalytic properties of BiOX can be enhanced by decreasing the thickness of 2D BiOX nanosheets.

However, due to the conduction band minimum (CBM) of BiOX photocatalysts was very positive [13–15], the photocatalytic reduction activity of BiOX was very low and there were only few reports on photoreduction of CO_2 using BiOX . On the other hand, theoretical reports showed that bismuth-rich strategy could increase the CBM potential of Bi-O-X photocatalysts. For instances, $\text{Bi}_{24}\text{O}_{31}\text{Br}_{10}$ could photocatalytically reduce Cr(VI) and split water [27], and $\text{Bi}_5\text{O}_7\text{I}$, $\text{Bi}_{24}\text{O}_{31}\text{Cl}_{10}$ and $\text{Bi}_3\text{O}_4\text{Br}$ could effectively activate molecular oxygen [28–31]. As a result, it was believed that thickness-ultrathin and bismuth-rich strategies would be good choices to improve the photocatalytic reduction properties of BiOX . Especially, ultrathin $\text{Bi}_x\text{O}_y\text{X}_z$ ($\text{X} = \text{Cl}, \text{Br}, \text{I}$) nanosheets photocatalysts should display a higher photocatalytic reduction activity than the counterpart BiOX .

Recently, solvothermal synthesis was usually used to prepare ultrathin BiOX nanosheets. The viscosity of solvent influenced the ion diffusion efficiency, which could regulate the crystal growth [16]. It has been reported that BiOX nanosheets could be synthesized by hydrothermal method using alcohol and ethylene glycol. As glycerol has higher viscosity than alcohol and ethylene glycol, it could possibly be used as the solvent to synthesize atomically thick two-dimensional BiOX crystals. However, as glycerol has a higher hydroxyl concentration, stable intermediates or products

could be generated, and it might not be hydrolyzed to produce BiOX nanosheets in less-water circumstance.

In this study, it was found that the solvothermal product was probably complex between bismuth, bromine and glycerol rather than BiOBr in glycerol system. Furthermore, the as-synthesized complex could be used as precursors to prepare $\text{Bi}_4\text{O}_5\text{Br}_2$ microspheres assembled by ultrathin nanosheets via a simple hydrolytic process (Fig. 1). As a new Bi-O-X photocatalyst, pure $\text{Bi}_4\text{O}_5\text{Br}_2$ was reported rarely [32,33]. In order to compare the photocatalytic reduction properties of $\text{Bi}_4\text{O}_5\text{Br}_2$ and BiOBr for solar energy generation, CO_2 photoreduction experiments were conducted. The photocatalytic results showed that the as-synthesized $\text{Bi}_4\text{O}_5\text{Br}_2$ samples displayed much higher photocatalytic reduction activity than BiOBr for CO_2 conversion. The excellent photocatalytic CO_2 reduction activity of $\text{Bi}_4\text{O}_5\text{Br}_2$ was caused by thickness-ultrathin and bismuth-rich strategies and the photocatalytic mechanism was also discussed in detail.

2. Experimental

2.1. Materials

$\text{Bi}(\text{NO}_3)_3 \cdot 5\text{H}_2\text{O}$, KBr , ethanol, cetyl trimethyl ammonium bromide (CTAB) and glycerol were analytically pure and purchased from Sinopharm Chemical Reagent Co., Ltd (Shanghai, China).

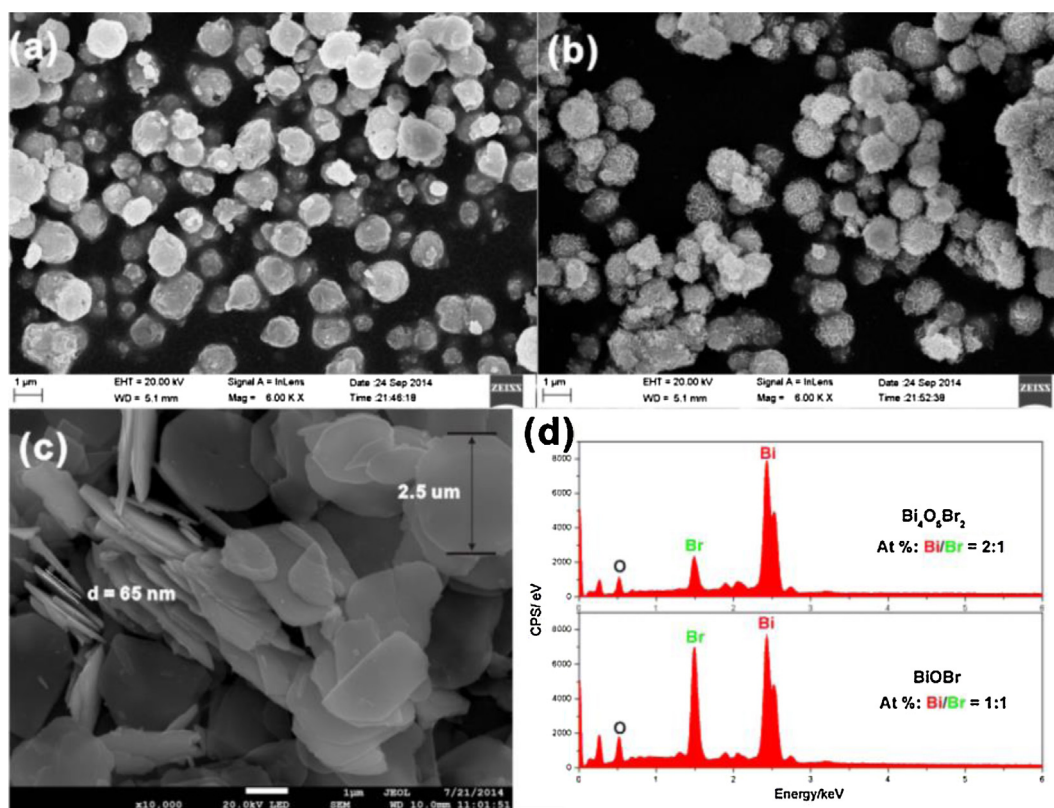


Fig. 3. FESEM images of complex precursor (a), $\text{Bi}_4\text{O}_5\text{Br}_2$ (b), BiOBr (c), and EDS spectra of $\text{Bi}_4\text{O}_5\text{Br}_2$ and BiOBr .

2.2. Synthesis

2.2.1. Complex precursor

KBr (2 mmol) was dissolved into 20 mL glycerol, and 2 mmol $\text{Bi}(\text{NO}_3)_3 \cdot 5\text{H}_2\text{O}$ was dissolved into another 20 mL glycerol. Then, KBr solution was added into the $\text{Bi}(\text{NO}_3)_3 \cdot 5\text{H}_2\text{O}$ solution drop by drop with continuously stirring. The suspension was transferred into Teflon-lined stainless steel autoclaves (50 mL) and kept at 160°C for 16 h. After reaction, the complex precursors precipitate was obtained by centrifugation, and then washed with ethanol. Finally, it was dried at 80°C under air atmosphere.

2.2.2. $\text{Bi}_4\text{O}_5\text{Br}_2$ microspheres

Complex Precursor (0.3 g) was dispersed in 100 mL deionized water. Then, $\text{Bi}_4\text{O}_5\text{Br}_2$ sample was obtained via a simple hydrolytic process, and washed successively with deionized water. Finally, it was dried at 80°C and thermal treatment at 200°C about 3 h.

2.2.3. BiOBr

The synthesis process is the same as that of complex precursors except using ethanol as solvent.

2.2.4. Ultrathin BiOBr

The synthesis process is the same as that of complex precursors except using ethanol as solvent and CTAB as bromine source.

2.3. Characterization

X-ray diffraction patterns (XRD) of the samples were recorded at room temperature (ca. 25°C) by a Bruker D8 advance X-ray diffractometer using $\text{Cu K}\alpha$ radiation and 2θ scan rate of 6 min^{-1} . Diffraction patterns were recorded over the 2θ range of $5\text{--}70^\circ$. Field emission scanning electron microscopic (FESEM) images were obtained by a Sigma Zeiss field emission scanning

electron microscope. Transmission electron microscopic (TEM) and high-resolution transmission electron microscopic (HRTEM) images were obtained by a JEOL JEM-2100 (RH) field emission Electron microscope. X-ray photoelectron spectroscopy (XPS) measurements were carried out by a Thermo ESCALAB 250XI X ray photoelectron spectrometer (Al K α , 150 W, C1s 284.8 eV). UV–vis diffuse reflectance spectra (DRS) were obtained using a UV–vis spectrometer (Perkin Elmer, Lambda 650s, BaSO_4 as a reference). Photoluminescence (PL) spectra (360 nm excitation) and time-resolved PL spectra (255 nm excitation) recorded by a FLS920 Multifunction Steady State and Transient State Fluorescence Spectrometer (Edinburgh Instruments room temperature). The Brunauer–Emmett–Teller (BET) surface areas were measured using a quantachrome autosorb-1 automated gas adsorption systems at 77 K.

2.4. Photocatalytic reduction of CO_2

The photocatalytic reduction of CO_2 was carried out in Labsolar-IIIAG closed gas system (Beijing Perfect Light Technology Co., Ltd, China). 1.3 g NaHCO_3 was added at the bottom of reaction (350 mL) firstly. Then, 0.15 g of the $\text{Bi}_4\text{O}_5\text{Br}_2$, ultrathin BiOBr or BiOBr was uniformly dispersed onto a watch-glass with an area of 28.26 cm^2 , and then the watch-glass was put in a reaction cell (Pyrex glass). Prior to the light irradiation, the above system was thoroughly vacuum-treated to remove the air completely, and then 5 mL 4 M H_2SO_4 was injected into the reactor to react with NaHCO_3 to achieve 1 atm CO_2 gas. After that, the reactor was irradiated from the top by a 300 W high pressure xenon lamp (PLS-SXE300C, Beijing Perfect Light Technology Co., Ltd, China) with 400 nm filter, and the photoreaction temperature was kept at 20°C by DC-0506 low-temperature thermostat bath (Shanghai Sunny Hengping Scientific Instrument Co., Ltd, China). During the irradiation, 1 mL of gas was taken from the reaction cell for subsequent qualitative analysis by

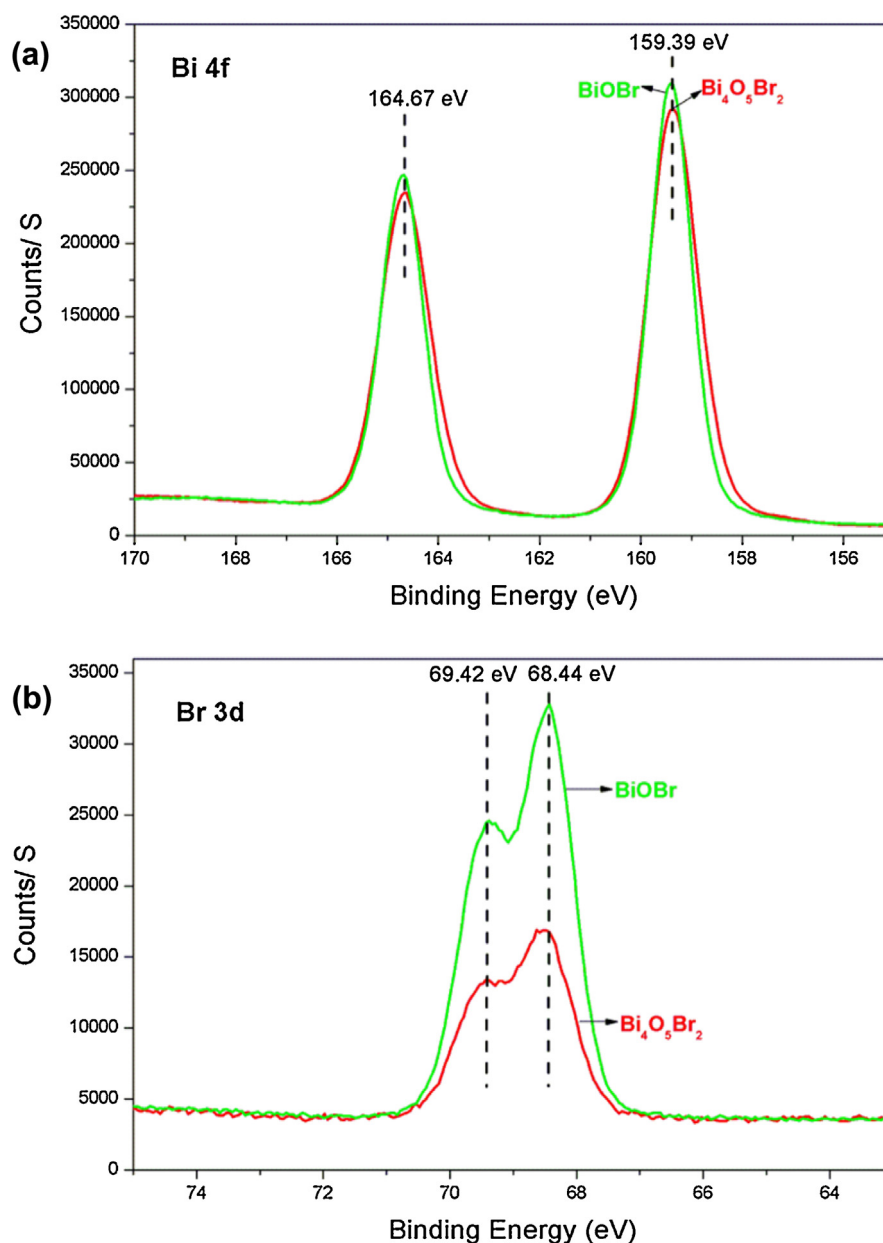


Fig. 4. High-resolution XPS spectra of Bi₄O₅Br₂ and BiOBr: (a) Bi 4f, and (b) Br 3d.

GC9790II gas chromatography (GC, Zhejiang Fuli Analytical Instrument Co., Ltd, China) equipped with a flame ionization detector (FID, GDX-01 columns). The quantification of the production yield was based on a calibration curve. The outlet gases were determined to be CO, CH₄ and CO₂.

The apparent quantum yields (AQY) was measured under the same photocatalytic reaction condition, except for the incident light wavelength. The solar fuels (CO and CH₄) yields of 1 h photoreaction under different monochromatic light wavelengths (420, 450, 475, 500, 525 and 550 nm) were measured. The band-pass and cutoff filters were used in the above measurement. AQY at different wavelengths is calculated by the following equation:

$$\text{AQY (\%)} = \frac{(\text{number of reacted electrons} / \text{number of incident photons}) \times 100\%}{[(2 \times \text{number of evolved CO molecules} + 8 \times \text{number of evolved CH}_4 \text{ molecules}) / \text{number of incident photons}] \times 100\%}$$

2.5. Theoretical calculation method

First-principles studies were carried out using plane-wave method as implemented in the Vienna ab initio simulation package (VASP) [34,35]. The Perdew-Burke-Ernzerhof (PBE) function with the generalized gradient approximation (GGA) was used to describe the ion-electron interaction and the core electrons were described by the full-potential projector augmented wave (PAW) method with an energy cutoff of 500 eV for the plane-wave expansion [36–38]. Geometry optimization was performed using the conjugate gradient algorithm until the force on each atom was less than 0.03 eV/Å, and the spin polarization was considered. Integrations in the Brillouin zone were performed using k-point grid generated with the Monkhorst-Pack grid.

3. Results and discussion

3.1. Catalyst characterization

Fig. 2 shows the XRD patterns of BiOBr (BET: $6.2 \text{ m}^2 \text{ g}^{-1}$), complex precursor, $\text{Bi}_4\text{O}_5\text{Br}_2$ (BET: $11.4 \text{ m}^2 \text{ g}^{-1}$), and the standard XRD pattern of PDF: 00-037-0699. For BiOBr, it was observed that the XRD pattern was in agreement with previously reported results [16], which were indexed with the standard tetragonal BiOBr structure (JCPDS 00-09-0393, space group: P4/nmm, unit cell parameters: $a = b = 0.3926 \text{ nm}$, and $c = 0.8103 \text{ nm}$). The XRD pattern of ultrathin BiOBr (BET: $13.7 \text{ m}^2 \text{ g}^{-1}$) was showed in Fig. S1. All the XRD peaks were indexed with BiOBr structure (JCPDS 00-09-0393). The larger half peak width of (001) peak indicated that the thickness of ultrathin BiOBr was much smaller than that of BiOBr. The XRD pattern of solvothermal product was not indexed in data base. However, $\text{Bi}_4\text{O}_5\text{Br}_2$ was obtained by hydrolyzing the solvothermal product. Therefore, the solvothermal product was called as complex precursor. For $\text{Bi}_4\text{O}_5\text{Br}_2$, it was observed that the XRD pattern was in agreement with the standard XRD pattern of PDF: 00-037-0699, with the standard monoclinic structure (space group: P21, unit cell parameters: $a = 1.452 \text{ nm}$, $b = 0.5625 \text{ nm}$, and $c = 1.083 \text{ nm}$, $\alpha = \gamma = 90.0^\circ$, $\beta = 97.6^\circ$).

The morphology and element information of $\text{Bi}_4\text{O}_5\text{Br}_2$ and BiOBr were shown in Fig. 3. It was found that complex precursor was in a structure of microsphere with a diameter of about $1 \mu\text{m}$. The microspheres were assembled by nanoparticles. After hydrolyzing, complex precursor was transformed into $\text{Bi}_4\text{O}_5\text{Br}_2$. As shown in Fig. 3b, the as-synthesized $\text{Bi}_4\text{O}_5\text{Br}_2$ were also microspheres with a diameter of about $1 \mu\text{m}$. However, the $\text{Bi}_4\text{O}_5\text{Br}_2$ microspheres were assembled by ultrathin nanosheets instead of nanoparticles. For comparison, the FESEM image of BiOBr is shown in Fig. 3c. The size of BiOBr nanosheets were about $2.5 \mu\text{m} \times 65 \text{ nm}$. In order to confirm the composition of $\text{Bi}_4\text{O}_5\text{Br}_2$, the energy dispersive spectrometer (EDS) characterization of $\text{Bi}_4\text{O}_5\text{Br}_2$ and BiOBr were compared as shown in Fig. 3d. It was observed that the Bi/Br atom ratio of $\text{Bi}_4\text{O}_5\text{Br}_2$ and BiOBr were 2:1 and 1:1, respectively. They were in agreement with their theoretical value, indicating that the XRD analysis was reliable.

In order to analyze the valence state of all atoms and to confirm the Bi/Br atom ratio of $\text{Bi}_4\text{O}_5\text{Br}_2$ and BiOBr, the XPS spectra of

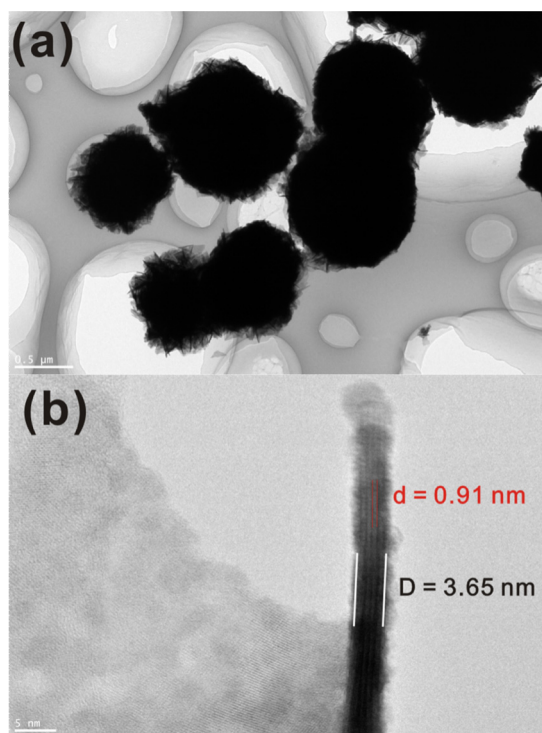


Fig. 5. Low-resolution TEM (a) and high-resolution TEM images, (b) of $\text{Bi}_4\text{O}_5\text{Br}_2$.

$\text{Bi}_4\text{O}_5\text{Br}_2$ and BiOBr are shown in Fig. 4. As shown in Fig. 4a, the XPS peaks of $\text{Bi } 4f_{7/2}$ and $\text{Bi } 4f_{5/2}$ of $\text{Bi}_4\text{O}_5\text{Br}_2$ and BiOBr were at 159.39 and 164.67 eV, respectively. It implied that Bi atoms in $\text{Bi}_4\text{O}_5\text{Br}_2$ and BiOBr were Bi^{3+} [39,40]. Fig. 4b shows the XPS peaks of $\text{Br } 3d$ of $\text{Bi}_4\text{O}_5\text{Br}_2$ and BiOBr. Two strong peaks at 69.42 and 68.44 eV were attributed to $\text{Br } 3d_{5/2}$ and $\text{Br } 3d_{3/2}$, respectively. It implied that Br atoms in $\text{Bi}_4\text{O}_5\text{Br}_2$ and BiOBr were Br^{-1} [29,30]. Furthermore, the peak areas of Bi 4f of $\text{Bi}_4\text{O}_5\text{Br}_2$ and BiOBr were equal. However, the Br 3d peak area of BiOBr was two times larger than that of $\text{Bi}_4\text{O}_5\text{Br}_2$. These results were in agreement with the atomic ratio of Bi/Br (2.1:1.0 for $\text{Bi}_4\text{O}_5\text{Br}_2$ and 1.0:1.0 for BiOBr), which were tested by X-ray photoelectron spectroscopy. More importantly, it indicated

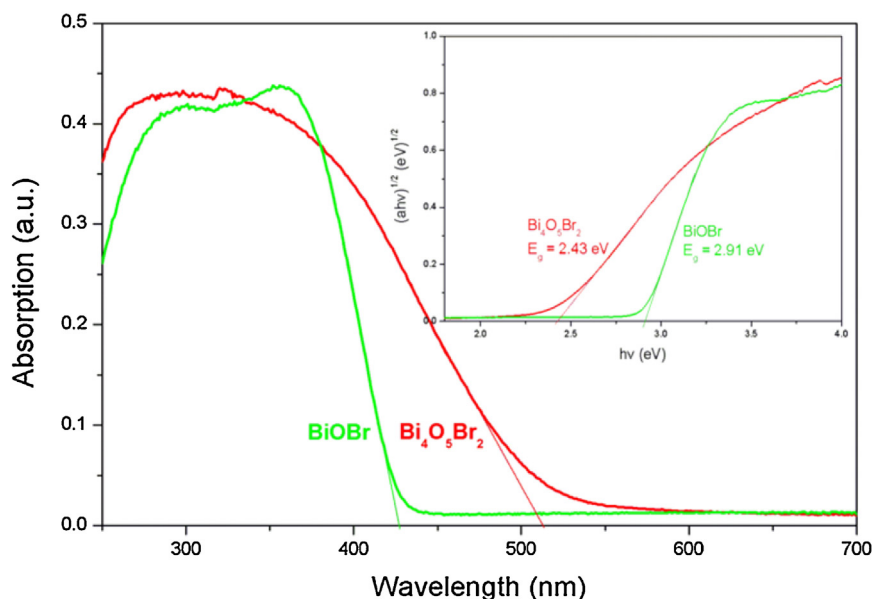


Fig. 6. UV-vis diffuse reflectance spectra of $\text{Bi}_4\text{O}_5\text{Br}_2$ and BiOBr.

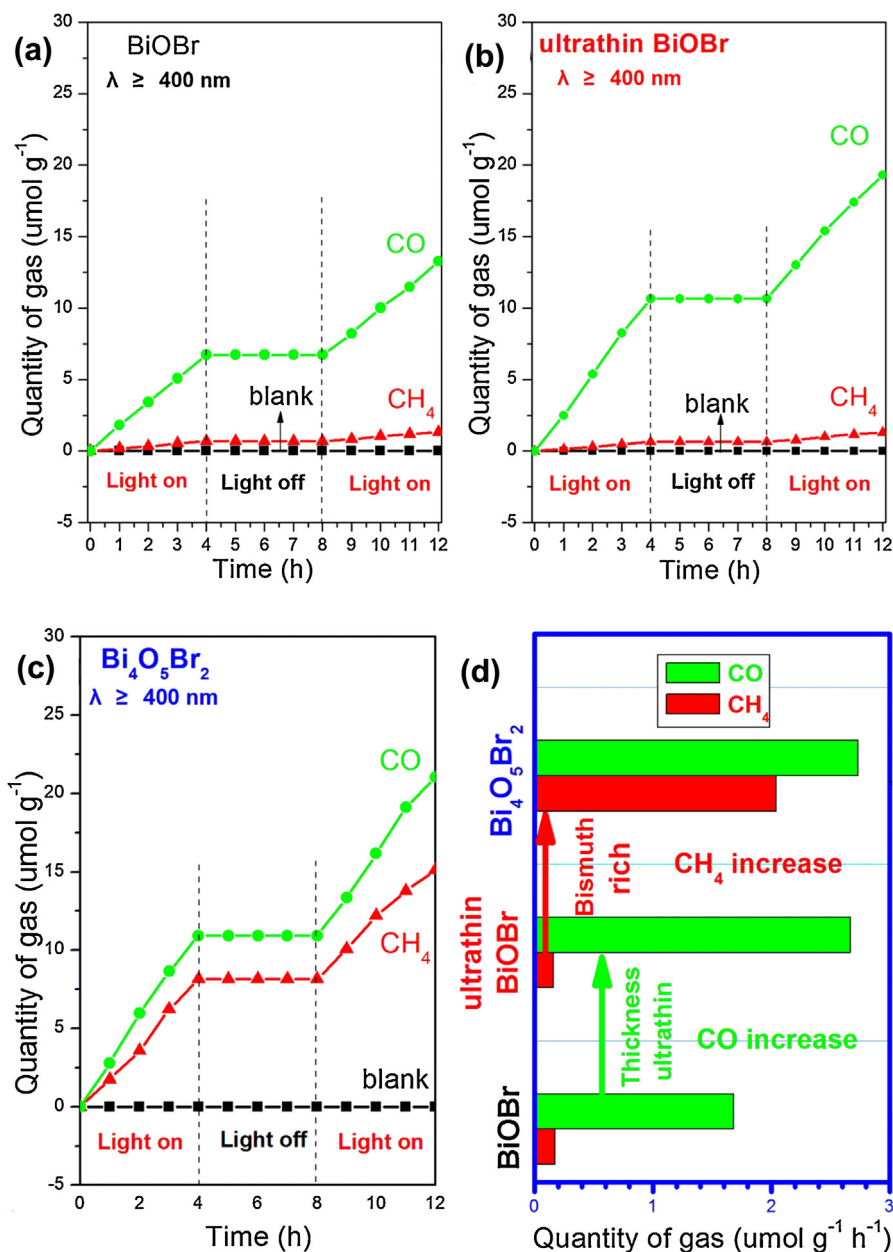


Fig. 7. Photocatalytic reduction activity for CO₂ conversion: (a) BiOBr; (b) ultrathin BiOBr; (c) Bi₄O₅Br₂ and (d) comparison of solar fuels generation.

that the as-synthesized Bi₄O₅Br₂ sample was a new bismuth-rich Bi-O-X photocatalyst.

The clear microsphere structure of Bi₄O₅Br₂ was displayed by TEM image (Fig. 5a). The size (ca. 1 μ m) and the second structure (ultrathin nanosheets) of Bi₄O₅Br₂ were the same as the SEM picture. The thickness was 3.65 nm, which was much less than that of BiOBr nanosheets (65 nm). It has been reported that BiOX had thickness dependent photocatalytic activity. For example, ultrathin BiOCl nanosheets (ca. 3 nm) showed higher photocatalytic activity than bulk BiOCl (30 nm) for H₂ generation [41]. Therefore, the ultrathin structure of Bi₄O₅Br₂ probably resulted in excellent photocatalytic reduction activity. Fig. 5b shows the high resolution TEM image of the side view of single Bi₄O₅Br₂ nanosheet. The lattice spacing of 0.91 nm was indexed to the {10-1} facets. It indicated that the two square facets (top and bottom facets) of Bi₄O₅Br₂ nanosheets were {10-1} facets, and the exposure percentage was more than 90%. Fig. S2 shows the TEM images of ultrathin BiOBr sample. It was observed that the thickness was about 3.9 nm and

the lattice spacing of 0.81 nm was indexed to the {001} facets of BiOBr.

Fig. 6 shows the UV-vis diffuse absorption spectra of Bi₄O₅Br₂ and BiOBr nanosheets. It was observed that Bi₄O₅Br₂ and BiOBr had absorption in the visible light region but different absorption edges. The absorption edge of Bi₄O₅Br₂ was about 510 nm, which was greater than that of BiOBr (425 nm). These results are consistent with the light yellow and yellow colors of BiOBr and Bi₄O₅Br₂, respectively. The band gap energy of BiOBr and Bi₄O₅Br₂ were evaluated by the following equation [16]:

$$\alpha h\nu = a(h\nu - E_g)^{n/2} \quad (1)$$

where α , h , ν , a , and E_g represent the absorption coefficient, planck constant, light frequency, energy-independent constant, and band gap (E_g values), respectively. For indirect transition of bismuth-based photocatalysts, n is 4 for BiOBr and Bi₄O₅Br₂. As shown in the inset of Fig. 6, E_g of Bi₄O₅Br₂ and BiOBr were estimated at about

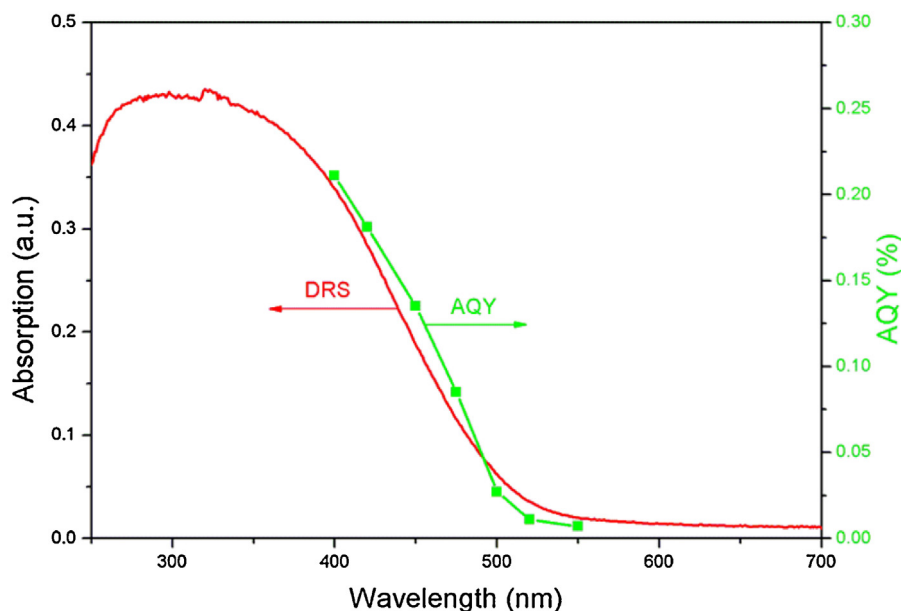


Fig. 8. Wavelength-dependent AQY and DRS spectra of $\text{Bi}_4\text{O}_5\text{Br}_2$.

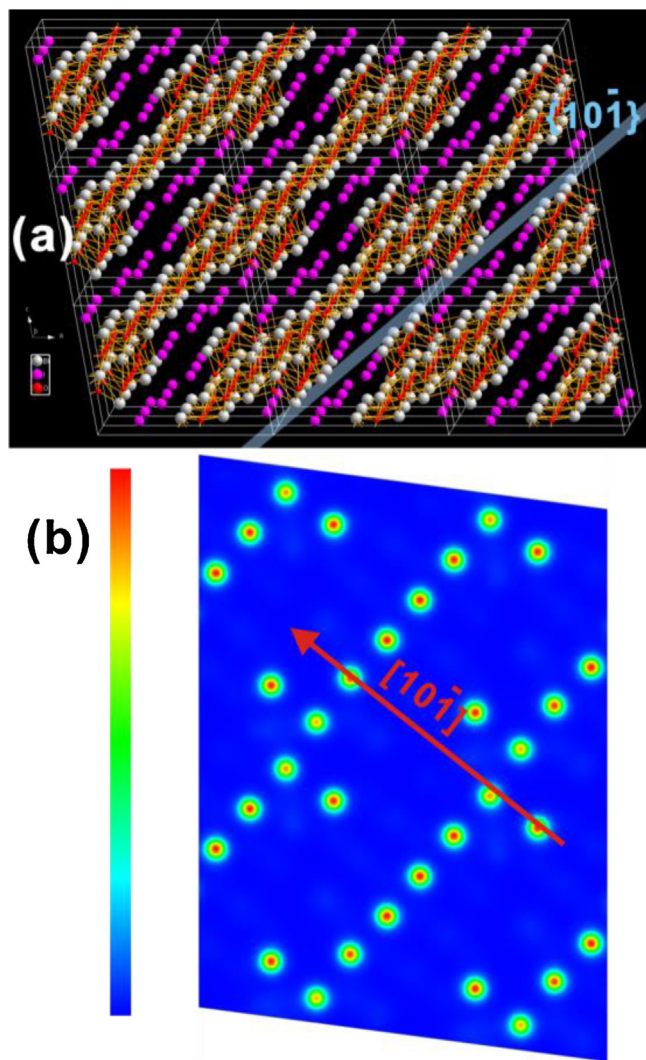


Fig. 9. The simulated structure (3×3) and charge density contour plots ($\{100\}$ surface) for $\text{Bi}_4\text{O}_5\text{Br}_2$.

2.43 and 2.91 eV, respectively. Therefore, $\text{Bi}_4\text{O}_5\text{Br}_2$ could be excited by visible light effectively.

3.2. Photoreduction of CO_2

At present, bismuth-based photocatalysts were rarely reported for photocatalytic reduction of CO_2 conversion [42,43]. The main reason is the low CBM, especially for BiOX . It was known that photocatalytic reduction activities depend on the CBM position. The lower the CBM resulted in lower the photocatalytic reduction activity. To adjust the CBM position of BiOX , some latest works showed that bismuth-rich strategy could advance the CBM position [27–31], with many relevant reports supported. Therefore, as a bismuth-rich Bi-O-X photocatalyst, $\text{Bi}_4\text{O}_5\text{Br}_2$ could be used for photoreduction of CO_2 into solar fuels. The control experiments (Figure S3) indicated that CO_2 could not be converted into energy gases (such as CH_4 or CO) without photocatalysts, light or CO_2 gases. And the H_2O -control data showed that H_2O was very important for CO_2 reduction. In the absence of H_2O , the CO production was decreased and no CH_4 was detected. When $\text{Bi}_4\text{O}_5\text{Br}_2$, ultrathin BiOBr or BiOBr was added, CO and CH_4 can be detected (Fig. 7). It was shown that the generation of CO and CH_4 by $\text{Bi}_4\text{O}_5\text{Br}_2$ is about 2.73 and $2.04 \mu\text{mol g}^{-1} \text{h}^{-1}$, which were much more than that by ultrathin BiOBr (CO : $2.67 \mu\text{mol g}^{-1} \text{h}^{-1}$; CH_4 : $0.16 \mu\text{mol g}^{-1} \text{h}^{-1}$) and BiOBr (CO : $1.68 \mu\text{mol g}^{-1} \text{h}^{-1}$; CH_4 : $0.17 \mu\text{mol g}^{-1} \text{h}^{-1}$). It indicated that the thickness-ultrathin and bismuth-rich strategies of Bi-O-Br improved the photocatalytic reduction activity intensely. However, thickness-ultrathin and bismuth-rich strategies played different roles. As shown in Fig. 7d, it was observed that thickness-ultrathin strategy increased the CO generation while bismuth-rich strategy increased the CH_4 generation. Namely, in $\text{Bi}_4\text{O}_5\text{Br}_2$ system, CO_2 was reduced to CO and CH_4 simultaneously in the presence of water vapor. After 4 h hibernation, $\text{Bi}_4\text{O}_5\text{Br}_2$, ultrathin BiOBr and BiOBr showed the same photocatalytic activity for CO_2 conversion when light on. Fig. S4 showed the effect of light intensity. It can be seen that the photocatalytic activity of $\text{Bi}_4\text{O}_5\text{Br}_2$ enhanced with the light intensity increasing. Furthermore, after four repeated experiments (Fig. S5), the generations of CO ($2.46 \mu\text{mol g}^{-1} \text{h}^{-1}$) and CH_4 ($1.93 \mu\text{mol g}^{-1} \text{h}^{-1}$) by $\text{Bi}_4\text{O}_5\text{Br}_2$ also were very high. It indicated that Bi-O-Br samples were stable photocatalysts for CO_2 photoreduction.

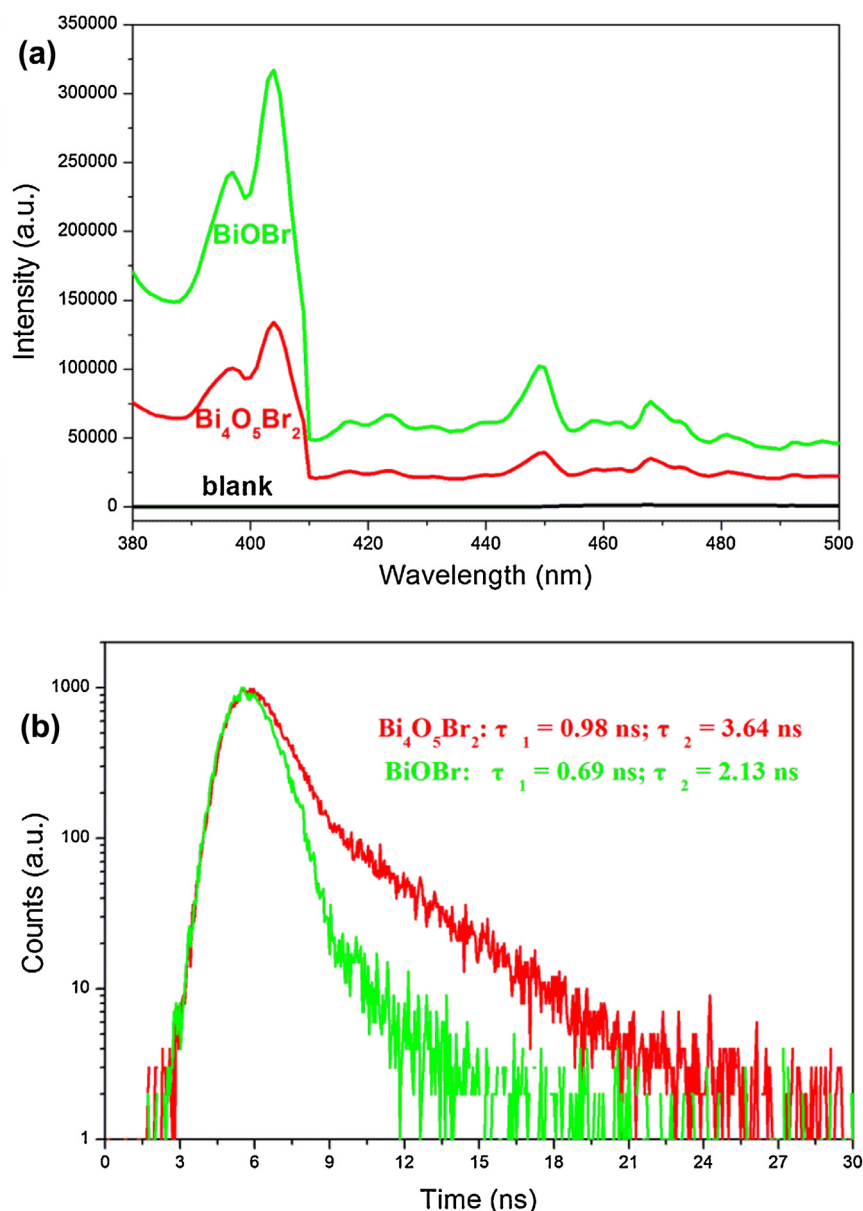


Fig. 10. PL and time-resolved PL spectra of $\text{Bi}_4\text{O}_5\text{Br}_2$ and BiOBr .

Fig. 8 shows the DRS spectrum of $\text{Bi}_4\text{O}_5\text{Br}_2$ along with the AQY of solar fuels (CO and CH_4) productions as a function of the incident monochromatic light wavelength. The AQY value showed a decreasing trend upon enhancing the wavelength of monochromatic light, which was consistent with the DRS spectrum. The AQY for the solar fuels (CO and CH_4) productions by $\text{Bi}_4\text{O}_5\text{Br}_2$ reached a maximum of 0.21% at 400 nm monochromatic light irradiation. It indicated that $\text{Bi}_4\text{O}_5\text{Br}_2$ microsphere assembled by ultrathin nanosheets could efficiently photoreduce CO_2 into solar fuels under visible light irradiation.

3.3. Photocatalytic mechanism

Fig. 9 shows the schematic diagram of $\text{Bi}_4\text{O}_5\text{Br}_2$ crystal structure. As BiOX , $\text{Bi}_4\text{O}_5\text{Br}_2$ had layered structure, which consisted of $[\text{Bi-O}]$ layers placed in between two slabs of bromine ions. However, the direction of layered crystal growth was $[10\bar{1}]$ direction, which was different from the $[001]$ direction of BiOX . Therefore, the direction of internal electric field of $\text{Bi}_4\text{O}_5\text{Br}_2$ was also different with BiOX . As

shown in Fig. 9b, the charge density surrounding $[\text{Bi-O}]$ layer was higher than that of double bromine slabs of $\text{Bi}_4\text{O}_5\text{Br}_2$. The homogeneous charge distribution between $[\text{Bi-O}]$ and double iodine slabs resulted in static electric field along $[10\bar{1}]$ axis by polarizing the related orbitals and atoms.

In previous works, it has been proved that the interlayer spacing and the thickness of Bi-O-X nanosheets can affect the internal electric field intensity along the layered crystal growth direction, leading to the different separation efficiency of photo-generated electrons and holes. The above TEM and SEM images showed that the thickness of layered $\text{Bi}_4\text{O}_5\text{Br}_2$ was much less than that of BiOBr . The interlayer spacing of $\text{Bi}_4\text{O}_5\text{Br}_2$ (namely d_{10-1} , 0.91 nm) was larger than that of BiOBr (namely d_{001} , 0.81 nm). Therefore, $\text{Bi}_4\text{O}_5\text{Br}_2$ had larger spatial polarization, which resulted in higher separation efficiency of photo-generated carriers than BiOBr . Fig. 10 displayed the PL spectra of $\text{Bi}_4\text{O}_5\text{Br}_2$ and BiOBr , which was used to estimate the separation efficiency of photo-generated carriers. The lower PL intensity of $\text{Bi}_4\text{O}_5\text{Br}_2$ implied that the separation efficiency of photo-generated carriers should be

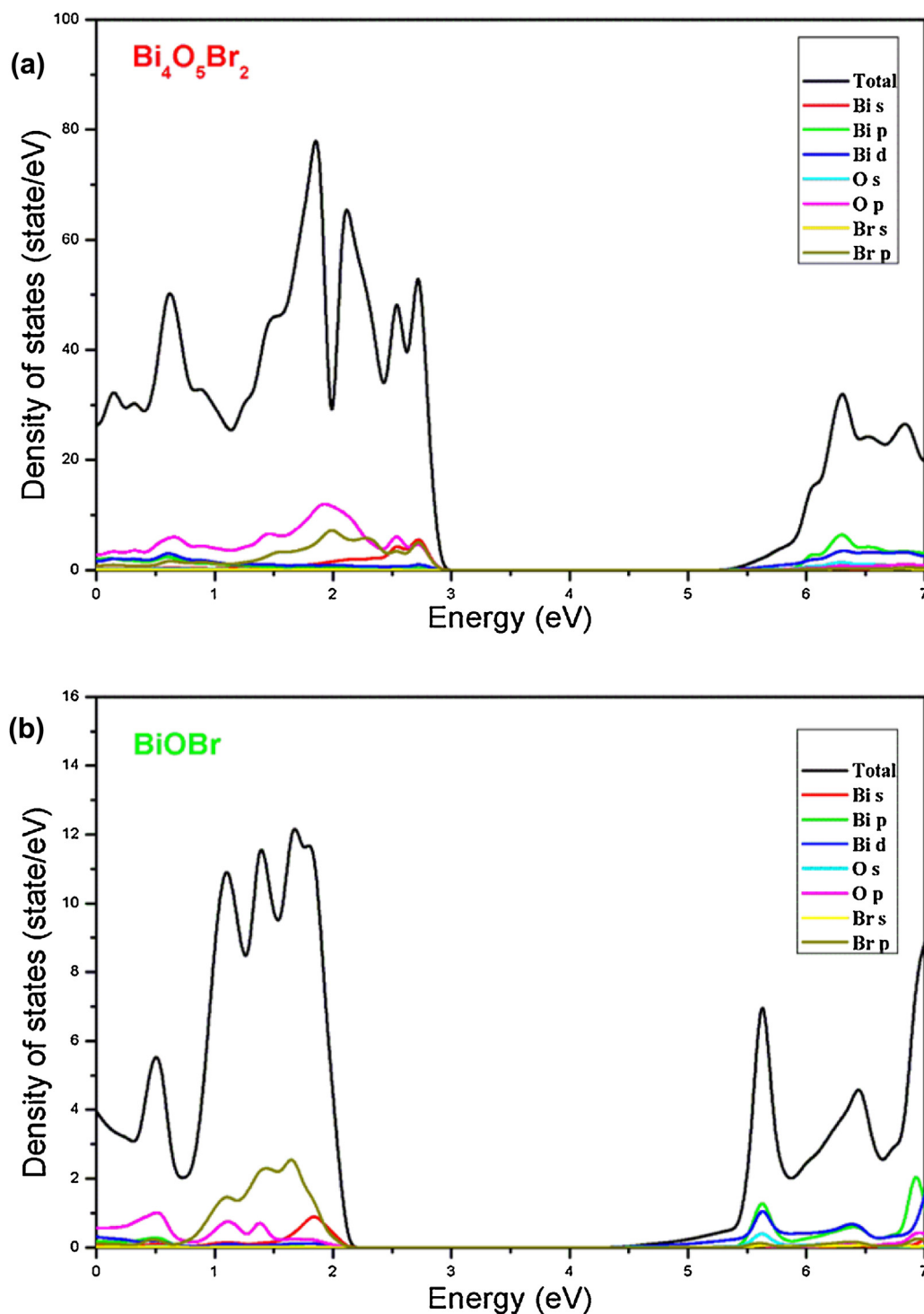


Fig. 11. Total DOS and partial DOS of $\text{Bi}_4\text{O}_5\text{Br}_2$ (a) and BiOBr (b).

higher than BiOBr [44]. In addition, the lifetime of charge carriers of $\text{Bi}_4\text{O}_5\text{Br}_2$ ($\tau_1 = 0.98$ ns; $\tau_2 = 3.64$ ns) also higher than that of BiOBr ($\tau_1 = 0.69$ ns; $\tau_2 = 2.13$ ns). This restricted lifetime also means the increased separation efficiency of photoinduced carriers by thickness-ultrathin and bismuth-rich strategies. Therefore, $\text{Bi}_4\text{O}_5\text{Br}_2$ showed higher photocatalytic activities for CO_2 conversion.

The above photocatalytic mechanism discussion started from the thickness-ultrathin of $\text{Bi}_4\text{O}_5\text{Br}_2$ nanosheets, which affected the separation efficiency of photo-generated carriers. Besides, the bismuth-rich strategy affected the CBM potential of Bi-O-Br. As

shown in Fig. 11, the theoretical calculation showed that the CBM of $\text{Bi}_4\text{O}_5\text{Br}_2$ was higher than that of BiOBr . This result was consistent with previous studies [41]. As a result, $\text{Bi}_4\text{O}_5\text{Br}_2$ had enhanced photocatalytic reduction activity for photoreduction of CO_2 into solar fuels under visible light irradiation.

4. Conclusions

In this study, $\text{Bi}_4\text{O}_5\text{Br}_2$ microsphere assembled by ultrathin nanosheets was synthesized via a glycerol precursor route and characterized by XRD, XPS, SEM, EDS, TEM, DRS and PL. Due

to the thickness-ultrathin and bismuth-rich strategies, $\text{Bi}_4\text{O}_5\text{Br}_2$ displayed an excellent photocatalytic reduction activity for CO_2 conversion under visible light irradiation. It indicated that $\text{Bi}_4\text{O}_5\text{Br}_2$ would be useful in energy and environmental photocatalysis fields. These findings could also deepen our understanding of enhanced the photocatalytic performances by single layered or few-layered bismuth-rich Bi-O-X photocatalyst over pure BiOX .

Acknowledgements

This work was supported by the National Natural Science Foundation of China (Nos. U1404506, 51502146), Natural Science Foundation of Henan Department of Science & Technology (No. 142102210477), Natural Science Foundation of Henan Department of Education (No. 14A150021), Natural Science Foundation of Nanyang Normal University (No. ZX2014039) to L Ye, and General Research Fund (GRF14100115) from Research Grant Council and ITSP Tier 3 Scheme (ITS/216/14) from Innovation Technology Commission of Hong Kong SAR Government. P.K. Wong was also supported by the CAS/SAFEA International Partnership Program for Creative Research Teams of Chinese Academy of Sciences, China.

Appendix A. Supplementary data

Supplementary data associated with this article can be found, in the online version, at <http://dx.doi.org/10.1016/j.apcatb.2016.01.044>.

References

- [1] H. Chen, C.E. Nanayakkara, V.H. Grassian, *Chem. Rev.* 112 (2012) 5919–5948.
- [2] C. Chen, W. Ma, J. Zhao, *Chem. Soc. Rev.* 39 (2010) 4206–4219.
- [3] W. Wang, J. Gong, *Front. Chem. Sci. Eng.* 5 (2011) 2–10.
- [4] F. Studt, I. Sharafutdinov, F. Abild-Pedersen, C.F. Elkjær, J.S. Hummelshøj, S. Dahl, I. Chorkendorff, J.K. Nørskov, *Nat. Chem.* (2014) 1873 (5pp).
- [5] Y. Ma, X. Wang, Y. Jia, X. Chen, H. Han, C. Li, *Chem. Rev.* 114 (2014) 9987–10043.
- [6] X. Wang, K. Maeda, A. Thomas, K. Takanabe, G. Xin, J.M. Carlsson, K. Domen, M. Antonietti, *Nat. Mater.* 8 (2009) 76–80.
- [7] X. Chen, S. Shen, L. Guo, S.S. Mao, *Chem. Rev.* 110 (2010) 6503–6570.
- [8] V.P. Indrakanti, J.D. Kubicki, H.H. Schobert, *Energy Environ. Sci.* 2 (2009) 745–758.
- [9] H. Zhang, J. Sun, V.L. Dagle, B. Halevi, A.K. Datye, Y. Wang, *ACS Catal.* 4 (2014) 2379–2386.
- [10] L. Liu, X. Chen, *Chem. Rev.* 114 (2014) 9890–9918.
- [11] F. Lei, Y. Sun, K. Liu, S. Gao, L. Liang, B. Pan, Y. Xie, *J. Am. Chem. Soc.* 136 (2014) 6826–6829.
- [12] K.L. Zhang, C.M. Liu, F.Q. Huang, C. Zheng, W.D. Wang, *Appl. Catal. B* 68 (2006) 125–129.
- [13] J. Jiang, L. Zhang, H. Li, W. He, J.J. Yin, *Nanoscale* 5 (2013) 10573–10581.
- [14] L. Ye, Y. Su, X. Jin, H. Xie, C. Zhang, *Environ. Sci.: Nano* 1 (2014) 90–112.
- [15] H. Cheng, B. Huang, Y. Dai, *Nanoscale* 6 (2014) 2009–2026.
- [16] X. Zhang, Z. Ai, F. Jia, L. Zhang, *J. Phys. Chem. C* 112 (2008) 747–753.
- [17] J.M. Song, C.J. Mao, H.L. Niu, Y.H. Shen, S.Y. Zhang, *CrystEngComm* 12 (2010) 3875–3881.
- [18] K. Zhao, L. Zhang, J. Wang, Q. Li, W. He, J. Jie Yin, *J. Am. Chem. Soc.* 135 (2013) 15750–15753.
- [19] L. Ye, L. Zan, L. Tian, T. Peng, J. Zhang, *Chem. Commun.* 47 (2011) 6951–6953.
- [20] J. Jiang, K. Zhao, X. Xiao, L. Zhang, *J. Am. Chem. Soc.* 134 (2012) 4473–4476.
- [21] L. Ye, J. Liu, C. Gong, L. Tian, T. Peng, L. Zan, *ACS Catal.* 2 (2012) 1677–1683.
- [22] L. Ye, C. Gong, J. Liu, L. Tian, T. Peng, K. Deng, L. Zan, *J. Mater. Chem.* 22 (2012) 8354–8360.
- [23] L. Ye, K. Deng, F. Xu, L. Tian, T. Peng, L. Zan, *Phys. Chem. Chem. Phys.* 14 (2012) 82–85.
- [24] X. Zhang, L. Zhang, *J. Phys. Chem. C* 114 (2010) 18198–18206.
- [25] L. Ye, J. Liu, Z. Jiang, T. Peng, L. Zan, *Appl. Catal. B* 142–143 (2013) 1–7.
- [26] M. Guan, C. Xiao, J. Zhang, S. Fan, R. An, Q. Cheng, J. Xie, M. Zhou, B. Ye, Y. Xie, *J. Am. Chem. Soc.* 135 (2013) 10411–10417.
- [27] J. Shang, W. Hao, X. Lv, T. Wang, X. Wang, Y. Du, S. Dou, T. Xie, D. Wang, *J. Wan, ACS Catal.* 4 (2014) 954–961.
- [28] L. Wang, J. Shang, W. Hao, S. Jiang, S. Huang, T. Wang, Z. Sun, Y. Du, S. Dou, T. Xie, D. Wang, *J. Wang, Sci. Rep.* 4 (2014) 7384 (8pp).
- [29] J. Wang, Y. Yu, L. Zhang, *Appl. Catal. B* 136–137 (2013) 112–1121.
- [30] Y. Su, H. Wang, L. Ye, X. Jin, H. Xie, C. He, K. Bao, *RSC Adv.* 4 (2014) 65056–65064.
- [31] X. Jin, L. Ye, H. Wang, Y. Su, H. Xie, Z. Zhong, H. Zhang, *Appl. Catal. B* 165 (2015) 668–675.
- [32] H.L. Chen, W.W. Lee, W.H. Chung, H.P. Lin, Y.J. Chen, Y.R. Jiang, W.Y. Lin, C.C. Chen, *J. Taiwan Inst. Chem. Eng.* 45 (2014) 1892–1909.
- [33] S.T. Huang, Y.R. Jiang, S.Y. Chou, Y.M. Dai, C.C. Chen, *J. Mol. Catal. A: Chem.* 391 (2014) 105–120.
- [34] G. Kresse, J. Hafner, *Phys. Rev. B* 47 (1993) 558–561.
- [35] G. Kresse, J. Furthmüller, *Phys. Rev. B* 54 (1996) 11169–11186.
- [36] J.P. Perdew, K. Burke, M. Ernzerhof, *Phys. Rev. Lett.* 77 (1996) 3865–3868.
- [37] P.E. Blöchl, *Phys. Rev. B* 50 (1994) 17953–17979.
- [38] G. Kresse, D. Joubert, *Phys. Rev. B* 59 (1999) 1758–1775.
- [39] Z. Ai, W. Ho, S. Lee, *J. Phys. Chem. C* 115 (2011) 25330–25337.
- [40] Z. Ai, W. Ho, S. Lee, L. Zhang, *Environ. Sci. Technol.* 43 (2009) 4143–4150.
- [41] L. Ye, X. Jin, Y. Leng, Y. Su, H. Xie, C. Liu, *J. Power Sources* 293 (2015) 409–415.
- [42] L. Zhang, W. Wang, D. Jiang, E. Gao, S. Sun, *Nano Res.* 3 (2015) 821–831.
- [43] Y. Zhou, Z. Tian, Z. Zhao, Q. Liu, J. Kou, X. Chen, J. Gao, S. Yan, Z. Zou, *ACS Appl. Mater. Interfaces* 3 (2011) 3594–3601.
- [44] Z. Zheng, B. Huang, J. Lu, X. Qin, X. Zhang, Y. Dai, *Chem. Eur. J.* 17 (2011) 15032–15038.